Scientific Research Publishing

Modeling and Numerical Simulation of Material Science, 2022, 12, 24-45
https://www.scirp.org/journal/mnsms
ISSN Online: 2164-5353
ISSN Print: 2164-5345

Modelling the Influence of Air Jet Configurations on Non-Woven Steel Fibre Mixing in the Melt Overflow Process

Ismail Abubakar[1], Hugh Gong[1], Sathish K. Nammi[2], Lee Marston[3], James Deane[3]

[1]School of Materials, University of Manchester, Manchester, UK
[2]Zienkiewicz Centre for Computational Engineering, Swansea University, West Glamorgan, UK
[3]Fibretech Limited, Pinxton, Nottingham, UK
Email: dr.ismail.abubakar@gmail.com

How to cite this paper: Abubakar, I., Gong, H., Nammi, S.K., Marston, L. and Deane, J. (2022) Modelling the Influence of Air Jet Configurations on Non-Woven Steel Fibre Mixing in the Melt Overflow Process. *Modeling and Numerical Simulation of Material Science*, **12**, 24-45.
https://doi.org/10.4236/mnsms.2022.122003

Received: March 7, 2022
Accepted: April 19, 2022
Published: April 22, 2022

Abstract

The mixing of non-woven steel fibres in melt overflow process for use in automotive muffler systems was simulated. The aim was to identify optimum parameters for achieving a good fibre mix. Numerical models of mixing chambers of melt overflow process were developed. Multiphysics analyses involving heat transfer, fluid flow and particle tracking were carried out using COMSOL code. The influence of air jet configurations on the fibre distribution was studied. The fibres settled on the moving bed within the mixing chamber were examined for their uniformity. The effect of additional air jets to the existing chamber in a range of regions was explored. An optimum configuration was identified by analyzing the compactness of the particle clusters deposited in the simulation and validated using pixel data acquired from real time imaging. The results showed that by employing dual air jets at the front end of the chamber, the density of the fibre material has improved. We conclude that through multi-physics modelling, it was possible to identify the optimum air-jet configurations leading to fibre uniformity and its distribution. This work also paves the way for incorporating a vision system to evaluate fibre density in real time.

Keywords

Non-Woven Steel Fibre, Steel Fibre Casting, Melt and Overflow, Pneumatic Conveying, Multi-Physics Simulation

1. Introduction

The exhaust gases from automobiles are a major source of air pollution. Auto-

mobiles discharge a range of toxic substances, such as nitrogen oxides (NOx), carbon monoxide and particulate matter (PM). This is a major concern for health and well-being. The air pollution also damages environment, reduces crop yields and contributes to adverse climate changes. There are stringent emission regulations within and outside of EU [1] [2] [3]. To meet these regulations, there is a need to improve exhaust systems of internal combustion engines. In this context, the automobile exhaust mufflers are crucial for emission control. A well-designed system also improves specific fuel consumption leading to reduced running costs. The automobile exhaust mufflers are mainly designed for two functions. The first is to add the exhaust system back-pressure, and thus improve efficiency. The second is for acoustic attenuation. Many works [4]-[10] have focused on improving muffler system design and configuration. The use of baffles in exhaust mufflers improves efficiency [11] [12] [13]. In this regard, the bulk of literature was on improving muffler and baffle designs. However, not much attention is reported on the effects of absorptive material wrappings around baffles for enhancing the efficiency and acoustic attenuation. The absorptive materials are commonly used to improve efficiency [14] [15]. Fibres made of glass and wool improve noise attenuation and thermal insulation with limited structural integrity [16]. The non-woven stainless steel wool fibres have noise attenuation features over a broad frequency range. They can maintain structural integrity in normal operational temperatures of internal combustion engines. In **Figure 1**, non-woven stainless steel wool fibres are shown which are fully recyclable and environment friendly. Its production involves melt and overflow procedure [17] [18] [19]. The manufacturing of these fibres involves usage of a refractory plunger which displaces downwards in the furnace. This causes molten metal to overflow into a specially designed rotating drum where it solidifies to form steel fibres. The steel fibres are accumulated in a collection chamber where they are mixed by air jets as illustrated in **Figure 2**. The steel wool is produced in the chamber and formed into a continuous roll. To acquire a uniformly packed wool of suitable density, a good fibre mixing is essential. The air jets within the chamber control the fibres trajectory and facilitate fibre mixing. The mixing effectiveness is paramount to achieve uniform fibre density. It is generally difficult to place a sensor or measurement device in the collection chamber to monitor real time data for optimising manufacturing process. This is mainly due to hot fibres becoming clogged in the machine leading to potential risk of explosion in high temperature and pressure environment of chambers. Thus, it is imperative to use modelling and simulation tools to understand temperature and pressure environment in chambers.

In this paper, the influence of air jet configuration on the melt and overflow process was investigated using multiphysics simulations thereby eliminating the need for instrumentation devices. Simulation facilitates optimising the chamber design for efficient fibre manufacturing. The aim was to identify configurations for improved density of non-woven steel wool. The COMSOL 5.3 Multiphysics code [20] was used throughout which is a tool for modelling and solving various

Figure 1. Non-woven steel wool fibres.

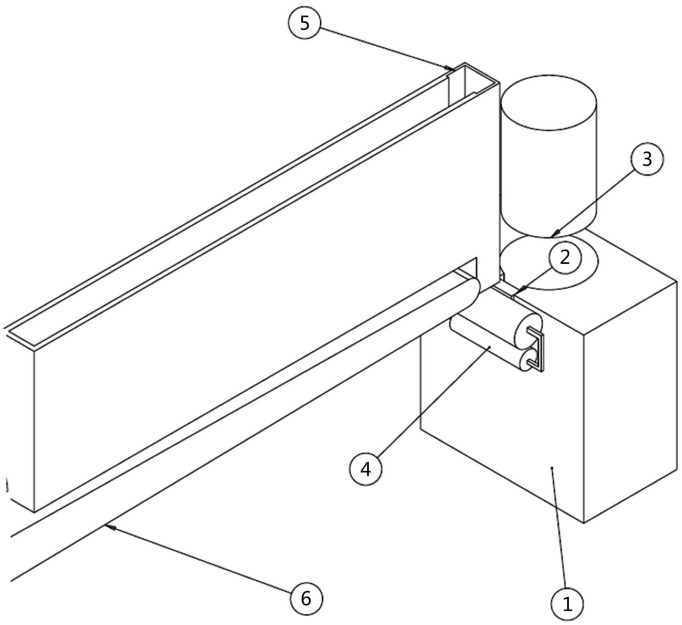

1	Furnace
2	Refractory lip
3	Plunger
4	Cast drum
5	Mixing chamber
6	Moving conveyor belt

Figure 2. Schematic of melt overflow process.

kinds of scientific and engineering problems based on Partial Differential Equations (PDE). These PDEs are solved using Finite Element Method (FEM) and run together with adaptive meshing and a variety of error control numerical solvers. The COMSOL has the ability to interrelate with different kinds of physics phenomena into single entity, thus offers flexibility and simplification of

modelling process. The work developed in this study is a step-by-step methodology that can be beneficial in exploring the effects of chamber design and air jet configurations. It was not possible to model fibres directly due to geometric complexity and limited computing power. Instead, spheroidal particles of effective volumes were used in numerical models to predict fibre distribution changes.

2. Mixing Chamber Modelling

The mixing chamber is a vital component in the fibre mesh production. Thus, it is desirable to have a mathematical representation of its overall mixing process. Steps involved in modelling the mixing (collection) chamber include building up mixing chamber space geometry, selection of physics module, assigning values and defining boundaries and meshing. In addition, Fibre modelling found in literature are simplified representations that do not consider structural transformation of fibres as it is spun [21] [22] [23] [24]. The modelling of fibre as it spins under transient boundary conditions is a challenge. Thus, to date there is no fully defined mathematical model that cover both melt over-flow process and mixing chamber with moving boundaries. As it was not possible to model fibres directly due to geometric complexity and limited computing power, spheroidal particles of effective volumes were used in numerical models to simulate fibre distribution. The simulation flowchart is shown in **Figure 3**. **Figure 4** is the 3D geometry of mixing chamber with a single jet at the front end. One face was exposed to atmosphere which is coloured in blue for visualisation.

3. Computational Study

The practical use of multi-physics modelling as an analysis tool for the mixing chamber is limited by the accuracy of the fluid flow models and the particle tracking procedures employed. The underlying assumptions employed in modelling are as follows:

- The base of the front end of the chamber is in a proximity to the furnace. This leads to a significant rise in the temperature of the fluid.
- The air jet pumps fluid is at a constant pressure. Thus, the velocity of the flow field varies across the mixing chamber.
- From the rig operator's experience, the volume fraction of fibre in background air of the mixing chamber is less than four percent.
- The trajectory of the casted fibres in the mixing chamber is affected by the momentum of the cast wheel, gravitational and drag forces experienced.

Tests were conducted at the plant rig in Fibretech Ltd., Pinxton. This was to measure fluid velocity inside the chamber in the absence of spun fibre filaments using a pitot tube. Readings were recorded at three locations across the length of the mixing chamber represented as Point-1, Point-2, and Point-3 as illustrated in the CAD model of **Figure 5**. The Pitot tube was positioned in a perpendicular manner to the airflow direction and readings were recorded three times in each

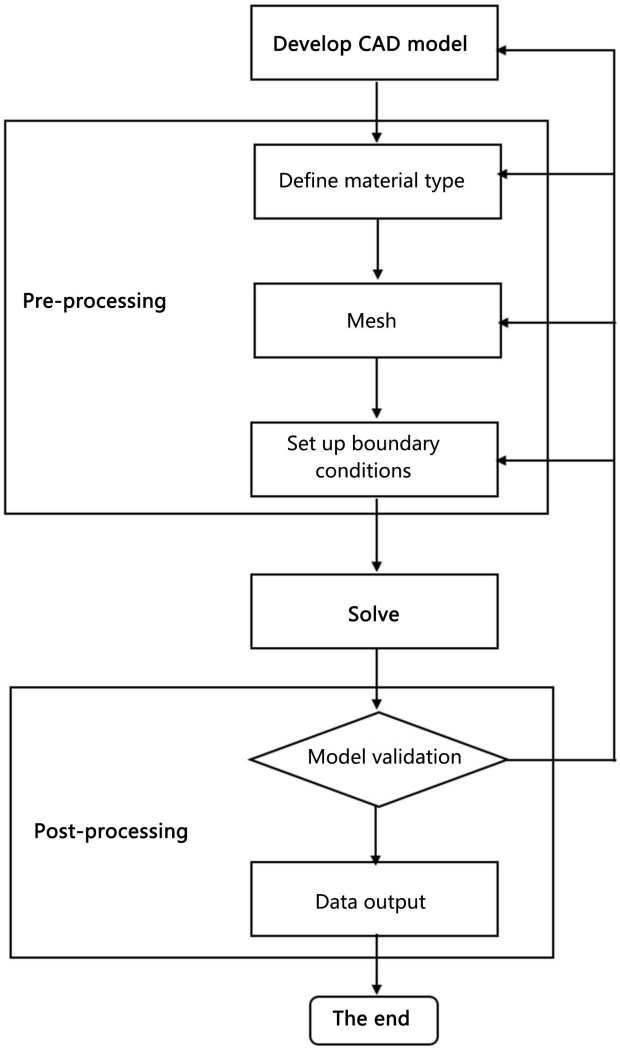

Figure 3. Flowchart of the study procedure.

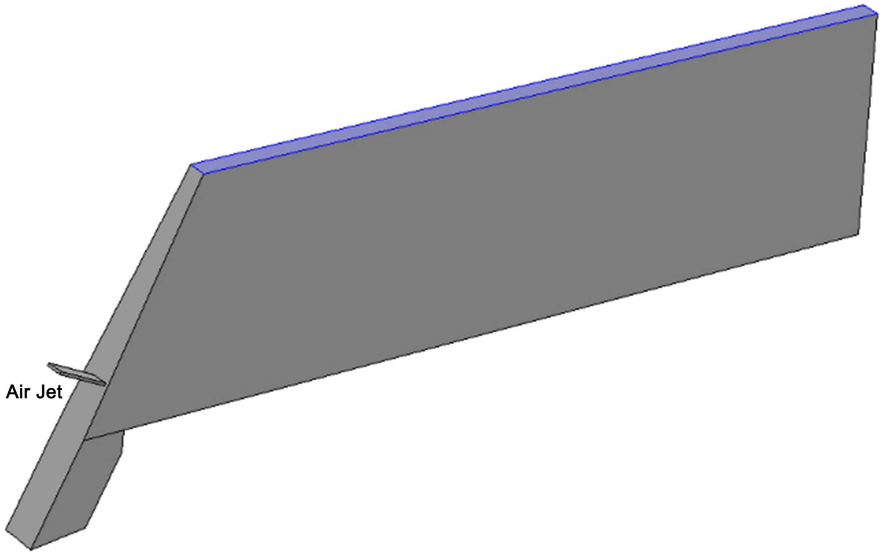

Figure 4. Initial chamber fluid domain.

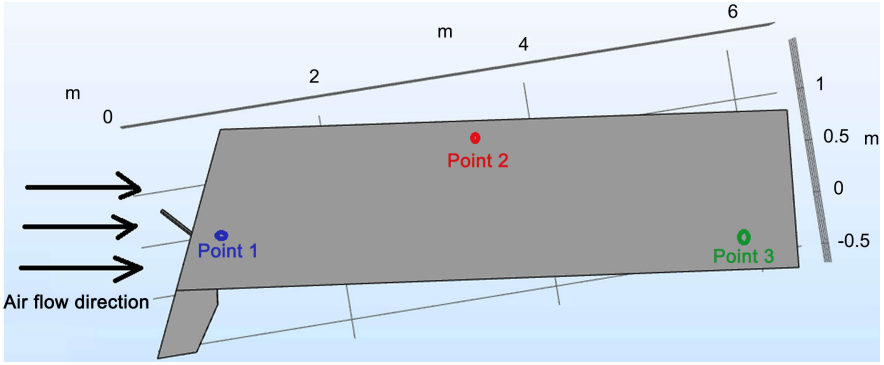

Figure 5. Air flow measurement regions.

position. The values are presented in Table 1. The measurements were carried out three times (at locations close to the two walls and the distance between them) and average values were noted as 28.63 m/s, 4.38 m/s and 2.10 m/s respectively. This information was used to guide the selection of suitable physics for the fluid field study. The flow Reynolds number was calculated using the following Equation (1):

$$R_e = \frac{\rho \cdot v \cdot D}{\mu} \tag{1}$$

A turbulent flow was assumed for $R_e > 2000$ and consequently turbulent physics models were considered for flow field simulations to estimate particle trajectories. After the physics had been established and the other properties such as fluid density and viscosity were automatically generated by the COMSOL 5.3 Multiphysics code [20]. The Finite Element Volume (FEM) based discretization of fluid domain is shown in Figure 6. The model was meshed with tetrahedral elements (including boundary layer elements). The order of the elements was set linear for the purpose of computing the velocity components. These elements are recommended for both laminar and turbulent phase flows in thermal analysis, and are numerically more stable [20]. It is worth to mention that a very coarse mesh will generate low quality mesh, which can cause large error in the simulation results. Conversely, if the mesh is too fine, the simulation will take longer computational time to arrive at an optimum solution. Thus, it is vital to decide a proper mesh configuration to arrive at a suitable solution within a reasonable computational time. Thus, a convergence study was carried out using coarse to extremely fine mesh. The temperature distribution along the length of the chamber was used as a benchmark to select optimum mesh size. It was decided to use a finer mesh density as shown in Figure 6.

3.1. Heat Transfer Analysis

The heat transfer of the air contained in the mixing chamber was computed. The air temperature in the chamber was measured experimentally under normal operating conditions. It was noted that the temperature variations across the 260.0 mm width of the chamber were negligible. The axial temperature variations

across the chamber are shown in Figure 7. A one-second time dependent heat transfer study was carried out and the measured temperature field was subsequently imposed on the fluid domain in the Computational Fluid Dynamics (CFD) simulation using Equation (2). It was assumed that the temperature field remained constant throughout the duration of the mixing process.

$$T(x) = 381.1e^{-1.475x} + 118.9e^{-0.067x} \quad (2)$$

Table 1. Measured airflow velocities for initial chamber design (case-1).

	Air velocity (m/s)			
Points	V1	V2	V3	V_mean
1	27.35	31.37	27.17	28.63
2	3.9	5.42	3.83	4.38
3	2.02	2.21	2.07	2.10

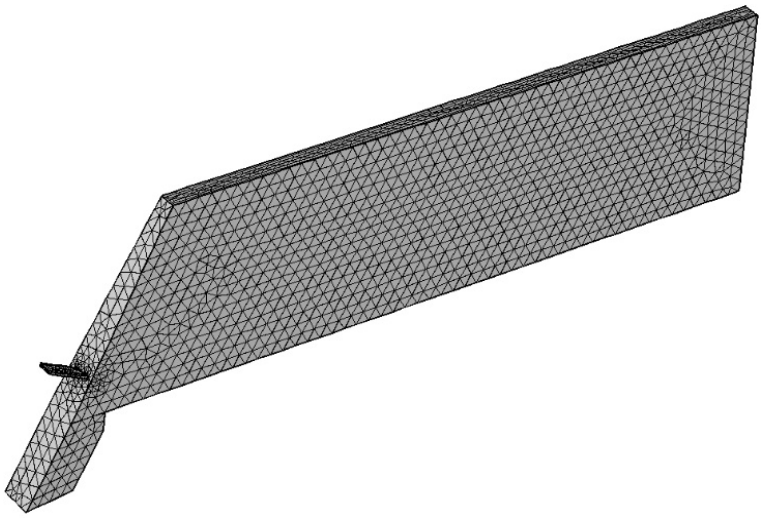

Figure 6. Discretised fluid domain.

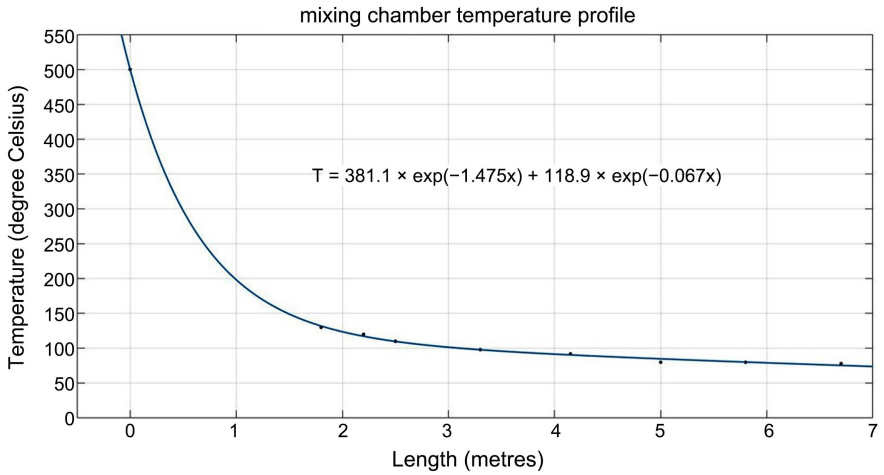

Figure 7. Experimentally measured temperature distribution along the mixing chamber length.

3.2. Flow Field Study

The air is continually pumped into the mixing chamber via the air jet. This is the compressible three-dimensional fluid studied here under a Mach number of 0.3. The numerical computation of the flow in a mathematical form is expressed by the conservation laws of fluid mechanics. The Navier-Stokes fundamental equation for the mass, momentum and energy conservation was applied for deriving formulations:

$$\frac{\partial \rho}{\partial t} + \nabla \cdot (\rho u) = 0 \tag{3}$$

$$\rho \frac{\partial u}{\partial t} + \rho (u \cdot \nabla) u = \nabla \cdot [-p + \tau] + F \tag{4}$$

$$\rho C_p \left(\frac{\partial T}{\partial t} + (u \cdot \nabla) T \right) = -(\nabla \cdot q) + \tau : S - \frac{T}{\rho} \frac{\partial p}{\partial t}\bigg|_p \left(\frac{\partial p}{\partial t} + (u \cdot \nabla) p \right) + Q \tag{5}$$

$$S = \frac{1}{2} \left(\nabla u + (\nabla u)^{\mathrm{T}} \right) \tag{6}$$

The Equations (3) and (4) represent conservation of mass and momentum respectively, and the Equation (5) describes the conservation of energy formulated in terms of temperature. These equations facilitate the physics and boundary condition specifications for the air flowing in the mixing chamber which were used for deriving the constitutive relations for Newtonian fluid. For the air flowing in the chamber, there exists a linear relationship between stress and strain. The dynamic viscosity μ depends on the thermodynamic state as per the following formulation.

$$\tau = 2\mu S - \frac{2}{3} \mu (\nabla \cdot u) \tag{7}$$

3.2.1. Turbulence Modelling

The air flow in the chamber is turbulent. Thus, the Navier-Stokes equations described in section 3.2 are supplemented by a turbulence model formulation. The k-ϵ model is adopted for time-dependent analysis here due to its good convergence rate with optimum computing memory [25]. The model introduces two additional transport equations and two dependent variables: turbulent kinetic energy (k) and turbulent dissipation rate (ϵ). The temperature dependent turbulent viscosity is in Equation (8).

$$\mu_T = \rho C_\mu \frac{k^2}{\epsilon} \tag{8}$$

The Equation (9) describes the transport equation for turbulent kinetic energy.

$$\rho \frac{\partial k}{\partial t} + \rho u \cdot \nabla k = \nabla \cdot \left(\left(\mu + \frac{\mu_T}{\sigma_k} \right) \nabla k \right) + P_k - \rho \epsilon \tag{9}$$

The production term is in Equation (10)

$$P_k = \mu_T \left(\nabla u : \left(\nabla u + (\nabla u)^{\mathrm{T}} \right) - \frac{2}{3} (\nabla \cdot u)^2 \right) - \frac{2}{3} \rho k \nabla \cdot u \tag{10}$$

The Equation (11) describes the turbulent dissipation-rate

$$\rho\frac{\partial\epsilon}{\partial t}+\rho u\cdot\nabla\epsilon=\nabla\cdot\left(\left(\mu+\frac{\mu_T}{\sigma_\epsilon}\right)\nabla\epsilon\right)+C_{\epsilon 1}\frac{\epsilon}{k}P_k-C_{\epsilon 2}\rho\frac{\epsilon^2}{k} \tag{11}$$

The model constants $C_\mu=0.09$, $C_{\epsilon 1}=1.44$, $C_{\epsilon 2}=1.96$, $\sigma_k=1.0$, $\sigma_\epsilon=1.3$ in Equations (8), (9), (10) and (11) were taken from experiments [26].

3.2.2. Boundary Conditions for the Flow Field Study

The temperature parameters were obtained from heat transfer analysis. These were then projected into the flow-field study for temperature effect on the process. A no slip boundary condition was assumed for the wall of the mixing chamber. That is, the air velocity relative to the chamber-wall is zero. The inlet boundary of the air jet was used to specify the net inflow into the domain. The gauge pressure in the air jet was measured as 11.46 kPa. This was used as the air pressure boundary condition at the inlet. The flow velocity and corresponding flow fields were then solved using a two-second time-dependent study. The purple-coloured surfaces highlighted in **Figure 8** were exposed to atmosphere.

3.3. Particle Trajectory Study

It is important to measure the fibre geometries to model the boundary condition correctly. The distribution of fibres within the mixing chamber influences the whole efficiency. The melt spun fibres typically range between 55 to 115 μm in diameter and up to 300 mm in length. The typical mass of a fibre ranges between 0.93 to 24.3 μg for non-woven steel of 7800 kg/m^3. Each of the particles is therefore assigned a mass of 12.6 μg which represents the average fibre mass. It is most convenient to express the geometry of an irregular fibre in terms of an equivalent diameter. In the analysis, the equivalent diameter of a fibre is taken as the diameter of a sphere with the same volume as the fibre itself. The fibre diameter as a function of its volume is expressed in Equation (12). This is a simplified formulation that neglects the true fibre geometry. However, the models can provide the scope and scale of the mixing within the chamber.

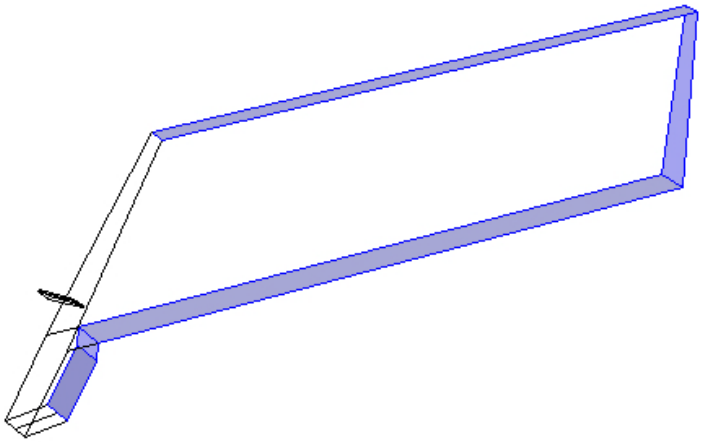

Figure 8. Chamber's exposed surface.

$$D_e = 3\sqrt{\frac{6V_p}{\pi}} \tag{12}$$

Particle Trajectory Study

The Lagrangian mechanics have been widely adopted by researchers to describe particle motions in a background fluid [27] [28] [29]. This approach allows the particles to be treated as distinct entities. The particle trajectory can be computed by solving differential equations using Newton's law of motion. The Equation (13) uses the particle mass and velocity. This is equal to the sum of the gravitational and drag forces. We have considered the influence of turbulent diffusion on the particles by using Standard drag correlation principle [30]. The drag force induced by fluid was calculated using Equation (14) and the particle velocity response time τ_p using Equation (15). The Discrete random walk model within Comsol code allows user to sample random perturbations to the background fluid velocity and use this to compute the drag force. This was used in conjunction with the gravitational force acting on the particle expressed in Equation (17).

$$\frac{\mathrm{d}}{\mathrm{d}t}\left(m_p v\right) = F = F_D + F_g \tag{13}$$

$$F_D = \left(\frac{1}{\tau_p}\right) m_p \left(u' - v\right); \quad u' = u + \Delta u \tag{14}$$

$$\tau_p = \frac{4\rho_p d_p^2}{3\mu C_D Re_\gamma} \tag{15}$$

$$Re_\gamma = \frac{\rho \left|u - v\right| D_p}{\mu} \tag{16}$$

$$F_g = m_p g\left(\frac{\rho_p - \rho}{\rho_p}\right) \tag{17}$$

A time dependent analysis of 5 seconds was used throughout the particle trajectory study for obtaining the final positions of the particles. To obtain accurate results, it is important to accurately represent the particle motions and their interaction with the fluid domain. After specifying the mass and equivalent diameter of the spheroidal particles, the velocity of the particles was given as input based on the cast wheel speed. This was obtained by assuming that the initial velocity of the fibres would be the same as the rotating cast wheel. Hence, the rotating speed of the cast wheel was measured and used as the initial velocity of the particles. To track the particle positions accurately, the particles in the inlet of the mixing chamber were partitioned into 2 portions, each having 100 particles and assigned a blue and red colour in each partition as illustrated in **Figure 9**. This helped to acquire a visual illustration of how well the particles mixed at the end of the study.

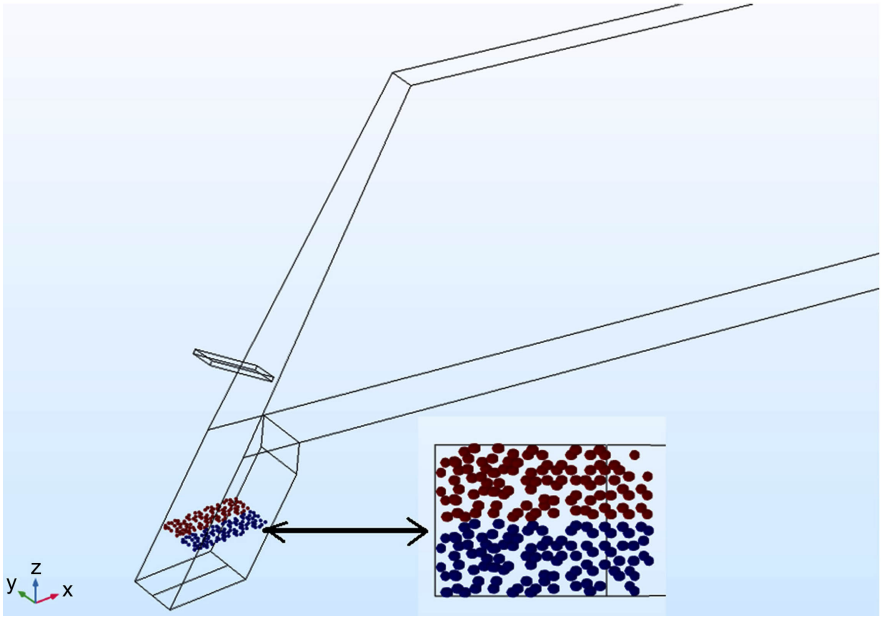

Figure 9. Particle entry into the mixing chamber.

3.4. Model Validation

Figure 10 presents the imposed temperature profile of the original mixing chamber using Equation (2) in conjunction with optimal mesh settings. The predicted flow fields for the study are shown as streamlines in Figure 11. The velocity of the air jet was above 80 m/s at the entrance, and progressively drops once inside the chamber to a value less than 5 m/s. The gradual drop was due to increment in chamber volume at a constant mass flow rate. The bigger the volume change, the greater the reduction in velocity. It can also be seen that there is a region of vorticity at the front of the chamber where the fluid rotates close to the air jet entrance. The values of average air velocity presented in Table 1 recorded at point 1, point 2, and point 3 were used to validate the simulation air velocity values in the chamber at similar positions. The values of the two velocities and their percentages difference are in Table 2. The correlation between the recorded average mean velocity and simulated values is checked using R^2 value. This is presented in Figure 12. The simulated velocity strongly correlates with the measured velocity as represented with the R^2 value close to unity. This justifies that the model is validated as a representation of the actual condition.

The particle trajectory is shown in Figure 13. It shows the progression of particles at the entrance of the mixing chamber through to the point of landing and settling on the conveyor belt. The particle trajectories and their corresponding distribution as they land and settle on the conveyor belt can be used to determine whether the flow conditions are beneficial to generate a well-mixed and uniformly distributed particle. Figure 14 shows a close-up view of the deposited particle cluster on the conveyor belt in the mixing chamber. A noticeable mixing between the blue and red particles was observed even though they were scattered. To verify the simulation results for particle deposition, fibres exiting

the mixing chamber of case-1 air jet configurations were captured in real-time on a white background and presented in Figure 15. The fibres represent the black pixels, and the white region (grey) represents the areas of void. As the fibres were conveyed out of the mixing chamber by the conveyor, there was a greater volume of mixing which mimics the actual experimentally observed outcomes.

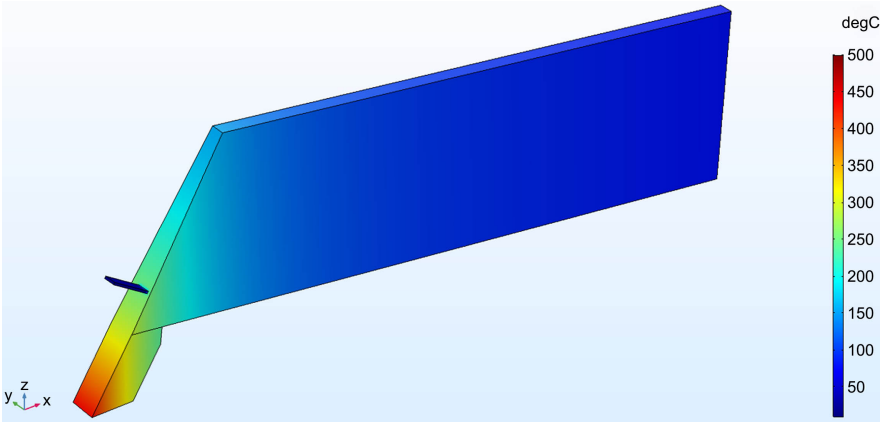

Figure 10. Temperature profile of the mixture chamber.

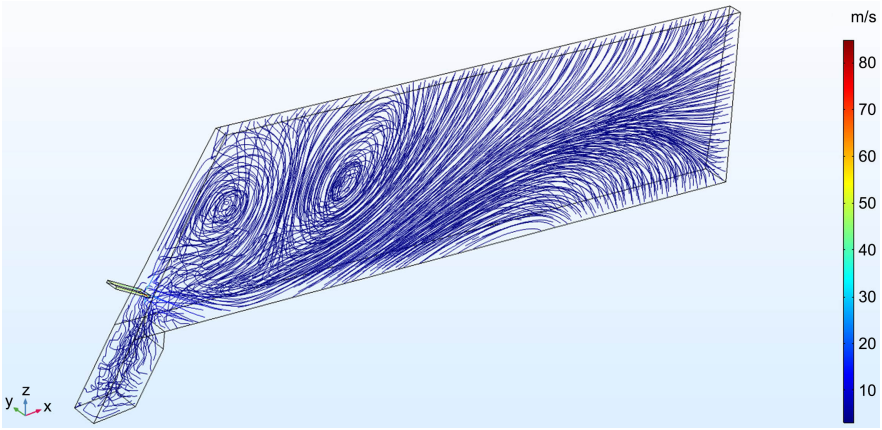

Figure 11. Predicted flow fields for initial chamber configuration.

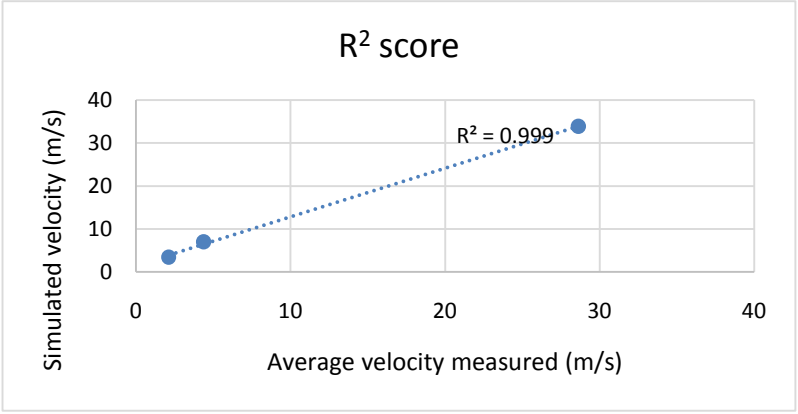

Figure 12. R^2 Score.

Table 2. Simulated and measured airflow velocities for initial chamber design (case-1).

	Air velocity (m/s)					
Points	V1	V2	V3	V_mean	Simulated velocity (m/s)	Percentage difference
1	27.35	31.37	27.17	28.63	33.88	18.33
2	3.9	5.42	3.83	4.38	5.98	36.53
3	2.02	2.71	2.07	2.28	3.34	46.50

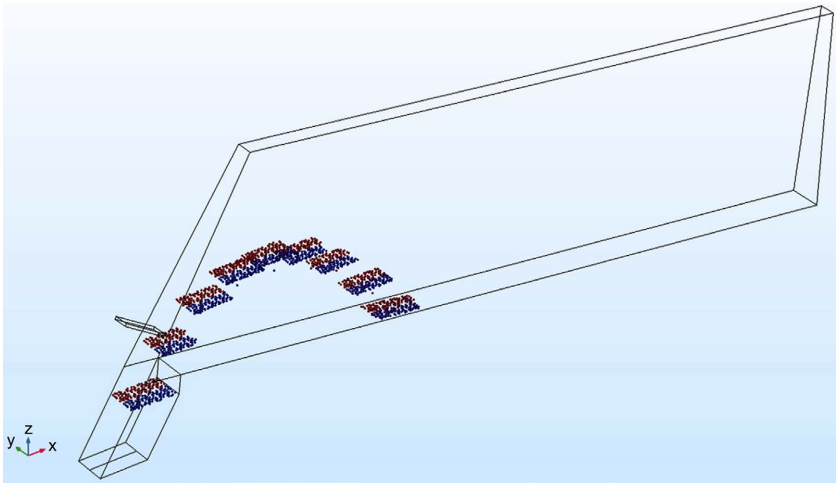

Figure 13. Predicted particles' trajectory for initial chamber configuration.

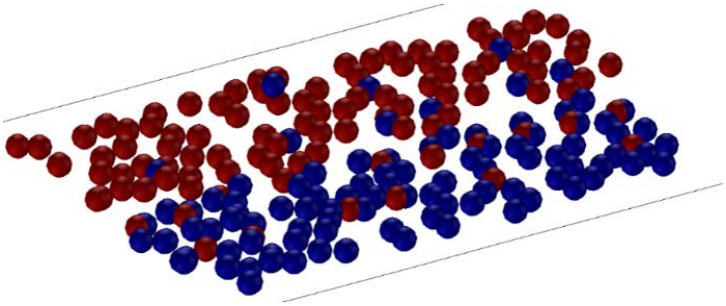

Figure 14. Predicted particle cluster deposited on the conveyer belt.

Figure 15. Captured fibres showing as pixels for the initial chamber design.

4. Results and Discussion

Table 3 summarizes all the variant air-jet configurations considered in the analyses. An additional simulation was carried out for these variants using the approach discussed in Section 3 keeping identical boundary conditions. The case-1 was the original configuration with a single air jet into the chamber. Three additional configurations (viz: case-2, case-3 and case-4) of the chamber set-up were simulated to maximise the fibre density using the same approach as case-1. The air-jets were positioned on the top, side and front for each of the three cases respectively. These cases are shown in Figure 16. The shaded surfaces in the figure were open to the environment. Figure 17(a), Figure 18(a) and Figure 19(a) show the predicted flow fields for case-2, case-3 and case-4 respectively. For case-1, with the addition of an extra air jet, the gas velocity exceeded the single air jet although rapidly dropped once inside the chamber to values of less than 10 m/s. The addition of an air jet in rest of the three cases has disrupted the vorticity that was present in case-1. In case-2, the additional air jet positioned at the top has no significant effect on the particle mixing as seen in Figure 17(c). The particle cluster formed is like the case-1 as shown in Figure 14. The additional air jet was positioned away from the zone where the particles land and settle. Hence, produced weak effect on the particle trajectory and mixing.

Table 3. Airjet configuration for case variants.

Case Number	Front Air Jet	Top Air Jet	Side Air Jet
1	1	-	-
2	1	1	-
3	1	-	1
4	2	-	-

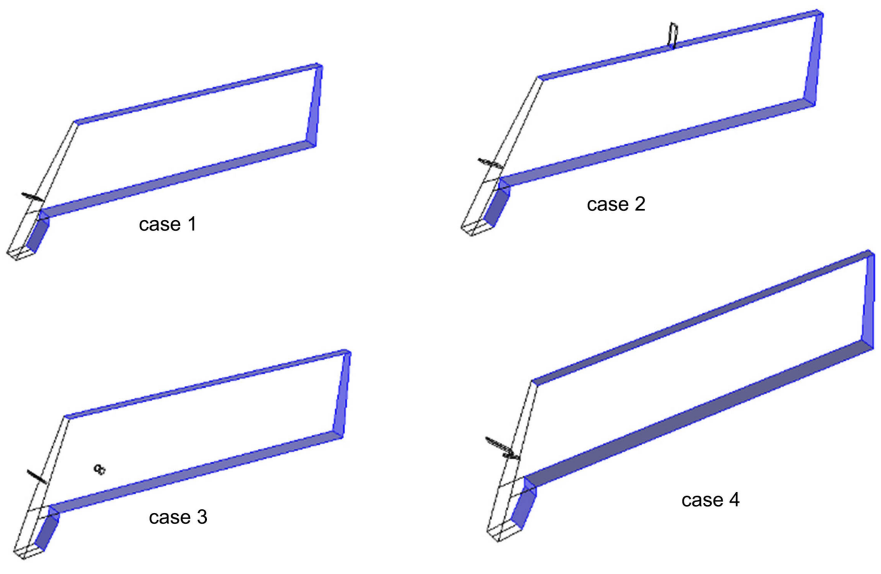

Figure 16. Varying air jet configurations.

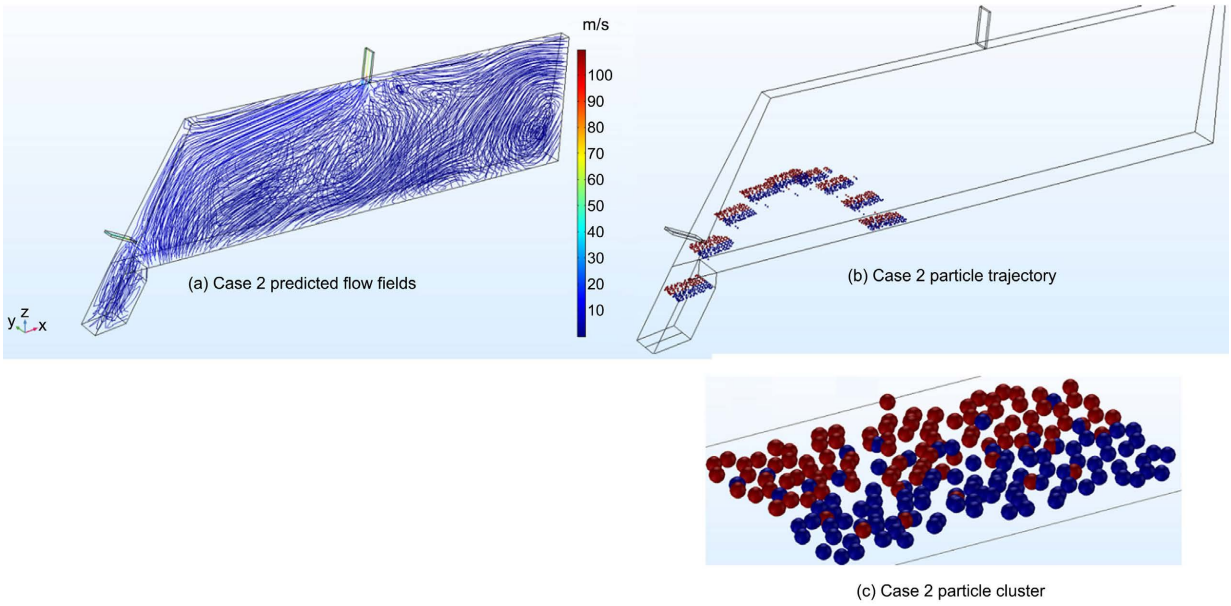

Figure 17. Case-2 simulation results.

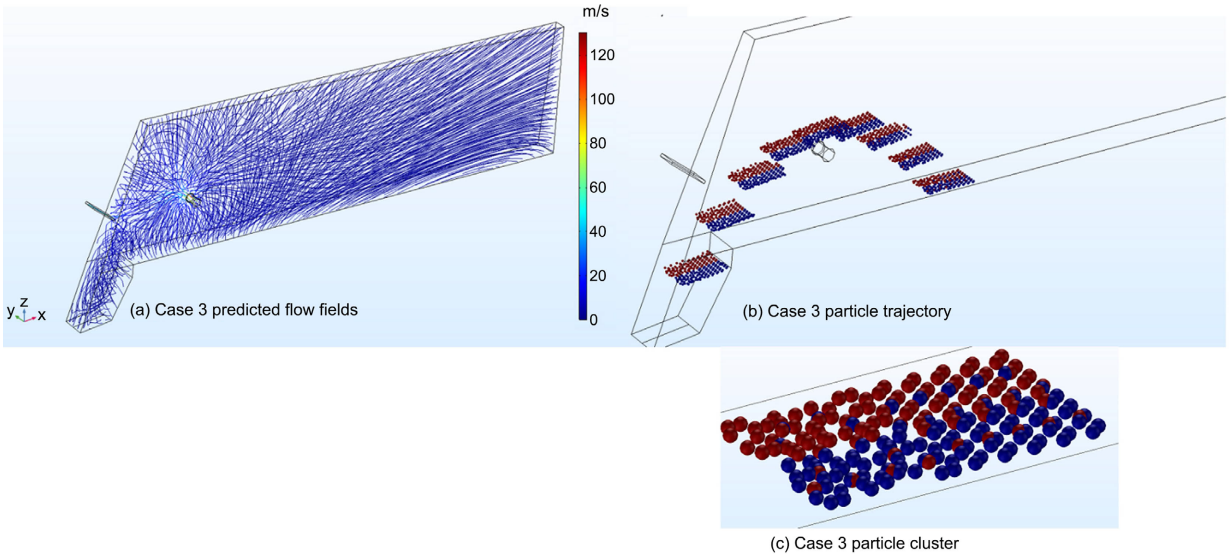

Figure 18. Case-3 simulation results.

In case 3, the addition of a side air jet introduced a swirling effect into the flow field at the front end that fades away across the length of the chamber. This effect yielded a better mix and produced a compact density in the particle cluster as seen in Figure 18(c). This effect was much more pronounced compared to case-1 and case-2. Further, a dispersed cluster was formed towards the entrance of the chamber where the swirling effect was at maximum. In case-4, the additional air jet was positioned symmetrically to the existing one (case-1). Both jets were configured to face each other thereby disrupting the flow field across the width of the chamber. The result produced the best particle cluster with an improved overall mixing as shown in Figure 19(c). The mixing chamber was modified to have an air jet configuration as simulated in case-4 which is shown in Figure 20.

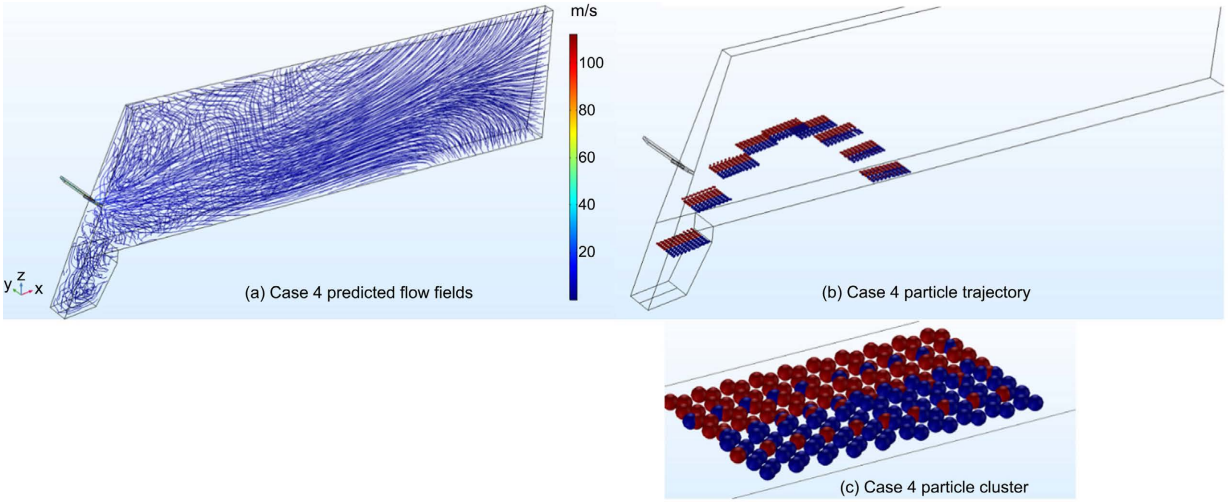

Figure 19. Case-4 simulation results.

Figure 20. Optimum air jet arrangement.

The fibre image exiting the collection chamber was captured in real time as shown in **Figure 21**. The result produced a denser image compared to that obtained from the initial study of case-1 shown in **Figure 15**. Image processing was carried out on the images captured for case-1 and case-4. A statistical probe was carried on the pixel intensity. A 1-bit pixel analysis was used. In such an analysis, the pixel values can either be black (0) or white (1), representing the darker and brighter areas of the image respectively [31]. The binary pixel data for case-1 and case-4 are presented in **Figure 22** and **Figure 23** respectively. The image of fibre mesh for case-1 produced black and white and pixels of 5.9×10^4 and 7.2×10^4 respectively. This is analogous to the predicted particle cluster of the simulation result in **Figure 14**. Conversely, the image captured for case-4 produced black and white pixels of approximately 8.4×10^4 and 4.7×10^4 mimicking the particle

cluster in Figure 19. In addition, the particle cluster appeared regular despite the turbulent flow because a freeze boundary condition was specified on the conveyor bed. This implies that particles that land on the conveyor become stuck to it. Also, the fluid pressure at the region where particles land on the conveyor is quite low to further displace the particles. To further validate the simulation approach in this work, five woven fibre samples were collected from the rig at air jet configurations of case 1 and case-4. The length of each sample was 100 mm and the masses were measured. Minimum mass, maximum mass and average mass for each case were calculated and presented in Table 4. As expected, steel fibre from case 1 produced minimum mass per 100 mm length (78.25 g) and case 4 produced the maximum mass (114.08 g). The average mass for case 1 is 86.00 g whilst case 4 produced 105.63 g.

Figure 21. Captured fibres shown as pixels to show the improved air jet configuration (case-4).

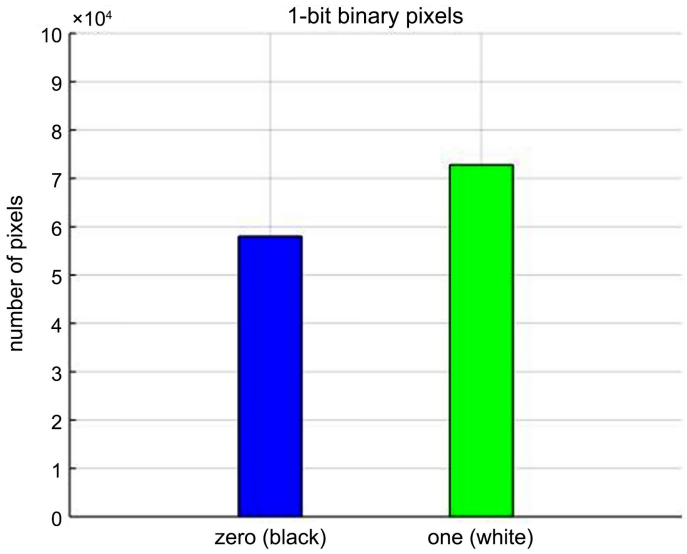

Figure 22. I-bit binary pixel data for case-I.

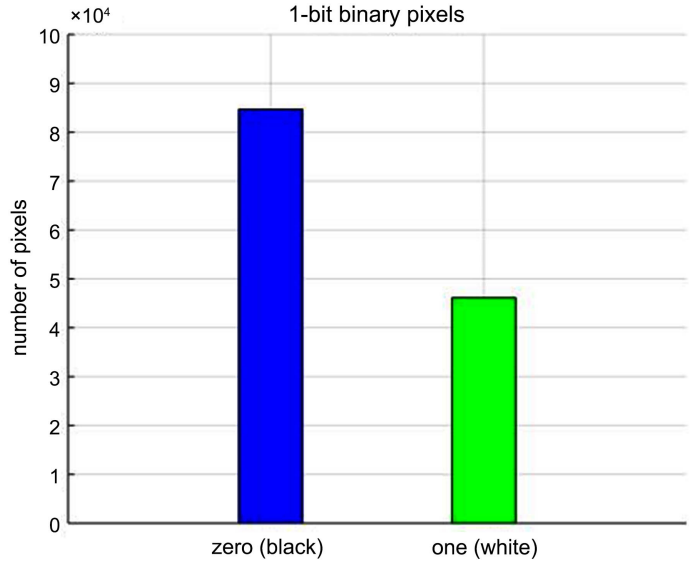

Figure 23. I-bit binary pixel data for case-4.

Table 4. Mass of samples collected.

	Mass in grams per 100 mm length	
	Case 1	Case 4
Sample 1	90.21	102.72
Sample 2	78.25	106.48
Sample 3	93.66	99.24
Sample 4	86.07	105.62
Sample 5	81.82	114.08
mean	86.00	105.63
min	78.25	99.24
max	93.66	114.08

5. Conclusion and Recommendations for Future Work

The flow fields and particle mixing inside a fibre collection chamber for a melt overflow casting process were simulated. Four configurations were studied. These scenarios mimic the equivalent particle diameters of a typical fibre produced from the experimental test setup. The simulations indicated that a simpler initial chamber set up models were useful for trial by error studies although they were not optimum configurations. We conclude that the optimisation studies were necessary for generating an adequate mixing of the casted fibres, mesh production and absorptive materials. In case-4 of our investigation, it was demonstrated that the introduction of an additional air jet at the front end of the chamber improves the fibre mixing across the width. The simpler formulation adopted for fibre representation neglected the true fibre geometry for the computational efficiency. This simulation was a precursor for assessing the likelihood and extent of fibre mixing for more complex studies. Initial set of simulations de-

termine a better air jet configuration in lieu of adopting a time-consuming trial by error approach.

Future wok shall introduce an appropriate design of experiment to further explore several combinations of the yaw and roll angles of the two front air jets of case-4 of our investigation that may produce the same or more improved fibre distribution.

Acknowledgements

We gratefully acknowledge the funding from Innovate UK No. 102792 that has helped to facilitate this project and allowed for significant design progress to be made. The authors would also like to thank Fibre Technology Ltd., Brookhill Road, Pinxton, UK for its contribution and commitment to the establishment of a melt overflow prototype collection chamber.

Conflicts of Interest

The authors declare no conflicts of interest regarding the publication of this paper.

References

[1] European Environmental Agency. Air Quality in Europe—2015 Report (EEA Report No. 5/2015). https://op.europa.eu/en/publication-detail/-/publication/9f0ff3b5-a4a5-11e5-b528-01aa75ed71a1/language-en

[2] European Commission. Commission Regulation 692/2008 of 18 July 2008 Implementing and Amending Regulation (EC) No. 715/2007 of the European Parliament and of the Council on Type-approval of Motor Vehicles with Respect to Emissions from Light Passenger and Commercial Vehicles.

[3] International Energy Agency (2017) CO_2 Emissions from Fuel Combustion. International Energy Agency, Paris.

[4] Dey, S. and Dhal, G.C. (2020) Controlling Carbon Monoxide Emissions from Automobile Vehicle Exhaust Using Copper Oxide Catalysts in a Catalytic Converter. *Materials Today*, **17**, 1-16. https://doi.org/10.1016/j.mtchem.2020.100282

[5] Bonnen, D., Bambad-Soufi, D., Steinkilberg, H. and Abram, K. (2014) Possibilities and Constraints for Lightweight in Exhaust Systems. SAE International, Graz. https://doi.org/10.4271/2014-01-2058

[6] Rajadurai, S., Afnas, M., Ananth, S. and Surendhar, S. (2014) Materials for Automotive Exhaust System. *International Journal of Recent Development in Engineering and Technology*, **2**, 82-89.

[7] Nazir, M.H., Khan, Z.A., Saeed, A. and Stokes, A. (2016) A Predictive Model for Life Assessment of Automotive Exhaust Mufflers Subject to Internal Corrosion Failure Due to Exhaust Condensation. *Engineering Failure Analysis*, **63**, 43-60. https://doi.org/10.1016/j.engfailanal.2016.02.014

[8] Liu, S.-J., *et al.* (2016) Intake and Exhaust System Performance of Diesel Engine Based on CFD and Steady Flow Test Method. *Chinese Society of Internal Combustion Engines*, **34**, 68-73.

[9] Xiao, G. (2015) Transient Simulation of Heat Transfers for Vehicle Exhaust System.

Procedia Engineering, **126**, 410-415. https://doi.org/10.1016/j.proeng.2015.11.233

[10] Barbieri, R. and Bariberi, N. (2006) Finite Element Acoustic Simulation Based Shape Optimisation of a Muffler. *Applied Acoustics*, **67**, 346-357. https://doi.org/10.1016/j.apacoust.2005.06.007

[11] Gupta, A.K. (2016) Observation for Transmission Loss by Applying Multiple Baffle Plates on Single Expansion Chamber: A Simulation Approach. *International Journal of Engineering Research and Modern Education*, **1**, 153-159.

[12] Elsayed, A., *et al.* (2017) Investigation of Baffle Configuration Effect on the Performance of Exhaust Mufflers. *Case Studies in Thermal Engineering*, **10**, 86-94. https://doi.org/10.1016/j.csite.2017.03.006

[13] Guhan, O.A.C., Arthanareeswaran, G., Varadarajan, K.N. and Krishnan, S. (2018) Exhaust System Muffler Volume Optimsation of Light Commercial Vehicle Using CFD Simulation. *Materials Today*, **5**, 8471-8479. https://doi.org/10.1016/j.matpr.2017.11.543

[14] Huff, N.T. (2001) Materials for Absorptive Silencer Systems. *Journal of Passenger Car*: *Mechanical Systems Journal*, **110**, 1680-1685. https://doi.org/10.4271/2001-01-1458

[15] Kalita, U., Pratap, A. and Kumar, S. (2015) Absorption Materials Used in Muffler: A Review. *International Journal of Mechanical and Industrial Technology*, **2**, 31-37.

[16] Reddy, A.K. (2017) A Critical Review on Acoustic Methods & Materials of a Muffler. *Materials Today*: *Proceedings*, **4**, 7313-7334. https://doi.org/10.1016/j.matpr.2017.07.061

[17] Johnson, E., Grabek, L., Johansen, A. and Kristensen, S.L. (1988) Microstructure of Rapidly Solidified Stainless Steel. *Material Science and Engineering*, **98**, 301-303. https://doi.org/10.1016/0025-5416(88)90174-7

[18] Gaspar, T.A. and Hackman, L.E. (1991) Melt Overflow Process for Direct Cast Fibre, Ribbon and Strip. *Materials Science and Engineering*, **A133**, 676-679. https://doi.org/10.1016/0921-5093(91)90160-O

[19] Herrera, C., de Lima, N.B., Kliagua, A.M. and Padilha, A.F. (2008) Microstructure and Texture of Duplex Stainless Steel after Melt-Spinning Processing. *Material Characterisation*, **59**, 79-83. https://doi.org/10.1016/j.matchar.2006.10.022

[20] COMSOL (2017) COMSOL Documentation.

[21] Andrzej, Z., Leszek, J. and Wasiak, A. (1998) Dynamic Modelling of Melt Spinning. *Computational and Theoretical Polymer Science*, **8**, 143-157. https://doi.org/10.1016/S1089-3156(98)00028-2

[22] Blanco-Rodríguez, F.J. and Ramos, J. (2011) Melt Spinning of Semi-Crystalline Compound Fibers. *Polymer*, **52**, 5573-5586. https://doi.org/10.1016/j.polymer.2011.09.041

[23] Rawal, A. and Mukhopadhyay, S. (2014) Melt Spinning of Synthetic Polymeric Filaments. In: Zhang, D., Ed., *Advances in Filament Yarn Spinning of Textiles and Polymers*, Woodhead Publishing, Cambridge, 75-99. https://doi.org/10.1533/9780857099174.2.75

[24] Feng, P., Pan, J., Ma, Q. and Yang, C. (2018) Studies on the Melt Spinning Process of Square 8-Hole Hollow Polyester Fibre. *Fibres and Textiles in Eastern Europe*, No. 129, 14-16. https://doi.org/10.5604/01.3001.0011.7297

[25] Verteeg, H.K. and Malalasekera, W. (2007) An Introduction to Computational Dynamics. The Finite Volume Method. 2nd Edition, Pearson Education, Essex.

[26] Wilcox, D.C. (1998) Turbulence Modelling for CFD. 2nd Edition, DCW Industries.

[27] Patankar, N.A. and Joseph, D.D. (2001) Langrangian Numerical Simulation of Particulate Flows. *International Journal of Multiphase Flow*, **27**, 1685-1706. https://doi.org/10.1016/S0301-9322(01)00025-8

[28] Elfasakhany, A. and Bai, X.S. (2018) Numerical and Experimental Studies of Irregular-Shape Biomass Particle Motions in Turbulent Flows. *Engineering Science and Technology, an International Journal*, **22**, 249-265. https://doi.org/10.1016/j.jestch.2018.10.005

[29] Leduc, S., Fredriksson, C. and Hermansson, R. (2006) Particle-Tracking Option in Fluent Validated by Simulation of a Low-Pressure Impactor. *Advanced Powder Technology*, **17**, 99-111. https://doi.org/10.1163/156855206775123539

[30] Walter, G.R. (2019) Review of the Empirical Correlations for the Drag Coefficient of Rigid Spheres. *Powder Technology*, **352**, 350-359. https://doi.org/10.1016/j.powtec.2019.04.075

[31] Gonzalez, R.C., Woods, R.E. and Eddins, S.L. (2009) Digital Image Processing Using MATLAB. 2nd Edition, Gatesmark Publishing, Knoxville.

Nomenclature

$T(x)$	Temperature reading at an axial distance (x)
ρ	Density (kg/m^3)
u	Velocity (m/s)
p	Pressure (N/m^2)
τ	Viscous stress tensor (N/m^2)
F	Volume force vector (N/m^3)
C_p	Specific heat capacity at constant pressure (J/kg·K)
T	Absolute temperature (K)
q	Heat flux vector (W/m^2)
Q	Heat source (W/m^3)
μ	Dynamic viscosity (kg/m·s)
μ_T	Temperature dependent turbulent viscosity (N/m^{2}s)
k	Turbulent kinetic energy (J)
ϵ	Turbulent dissipation rate
P_k	Production term
D_e	Equivalent diameter of fibre (m)
V_p	The volume of the fibre (m^3)
m_p	The particle mass (kg)
v	The particle velocity (m/s)
F_D	The drag force by the fluid (N)
τ_p	The particle velocity response time (s)
ρ_p	Particle density (kg/m^3)
d_p	Particle diameter (m)
F_g	The gravitational force acting on the particle (m/s^2)
g	The gravitational constant (m/s^2)
R_e	Reynold Number (Dimensionless)
v_a	Velocity of air (m/s)
D	Characteristic of length (m)
S	Shear rate
C_μ	Turbulence model constant
C_D	Drag coefficient dependent of Relative Reynolds Number
σ_k	Turbulence kinetic energy constant
σ_ϵ	Turbulence dissipation rate constant
$C_{\epsilon 1}$	Turbulence transport equation constant1
$C_{\epsilon 2}$	Turbulence transport equation constant2
u	The mean flow velocity
Δu	The instantaneous perturbation velocity
u'	The sum of the mean field and the instantaneous perturbation
Re_γ	Relative Reynolds Number